MNRAS 000, 1–14 (2019) Preprint 15 June 2020 Compiled using MNRAS LATEX style file v3.0

On testing CDM and geometry-driven Milky Way rotational curve models with Gaia DR2

Mariateresa Crosta, [1]★ Marco Giammaria, [1,2] Mario G. Lattanzi, [1] Eloisa Poggio[1]
[1]*INAF - OATo, Turin, Italy*
[2]*UNITo, Dep. of Physics, Univ. of Turin, Italy*

Accepted XXX. Received YYY; in original form ZZZ

ABSTRACT

Flat rotation curves in disk galaxies provide the main observational support to the hypothesis of surrounding dark matter. Despite of the difficulty in identifying the dark matter contribution to the total mass density in our Galaxy, stellar kinematics, as tracer of gravitational potential, is the most reliable observable for gauging different matter components. From the Gaia DR2 catalog, we extracted parallaxes, proper motions and line-of-sight velocities of unprecedented accuracy for a carefully selected sample of disk stars. This is the angular momentum supported population of the Milky Way that better traces its observed rotation curve. We fitted such data to both a classical, i.e. including a dark matter halo, velocity profile model and a general relativistic one derived from a stationary axisymmetric galaxy-scale metric. The general relativistic Milky Way rotation curve results statistically indistinguishable from its state-of-the-art dark matter analogue. This supports the ansatz that a weak gravitational contribution due to the off-diagonal term of the metric, by explaining the observed flatness of Milky Way's rotation curve, could fill the gap in a baryons-only Milky Way, thus rendering the Newtonian-origin dark matter a GR-like effect. In the context of Local Cosmology, our findings are suggestive of the Galaxy's phase-space as the exterior gravitational field in equilibrium far from a Kerr-like inner source, possibly with no need for extra-matter to account for the disk kinematics.

Key words: gravitation – Galaxy: kinematics and dynamics – Galaxy: disk – dark matter– astrometry – catalogues

1 INTRODUCTION

The few-micro-arcsecond level (μas) of the Gaia measurements (Gaia Collaboration 2016, 2018) requires a fully general-relativistic analysis of the inverse ray-tracing problem, from the observational data (e.g., stellar images on a digital detector) back to the positions of light-emitting stars (Crosta et al. 2017, and references therein). This is because the Gaia-observer is embedded in the ever present and ever changing overlapping weak local gravitational fields of the Solar System. Once the observer is properly defined, null geodesics represent the real physical link through space-time up to the stars. This is the framework of modern Relativistic Astrometry. In this respect, the weak gravitational regime is playing a pivotal role in providing a complementary observational perspective for understanding gravity. Moreover, once a relativistic model for the data reduction is in place, any subsequent scientific exploitation should be consistent with that model.

By routinely scanning individual sources throughout the whole sky, Gaia directly measures the kinematics of the stellar component of the Milky Way (MW). Gaia's second data release (DR2, Gaia Collaboration 2018) is the first of its deliveries providing parallaxes and annual proper motions, to $\sim$ 100 μas (for the brighter stars), for about 1.3 billion of the objects surveyed. It also includes Gaia-measured radial velocities (RVs), although for "only" 7 million stars with estimated effective temperatures between 3550 and 6900 K (Katz et al. 2019).

Our work is the first attempt to apply the relativistic kinematics delivered by Gaia to trace the flat Galactic rotation curve (RC) at large radii from its center.

This flatness has been explained as a deviation from the Newtonian velocity profile because of the presence of dark matter (Zwicky 1937; Rubin, Thonnard & Ford 1978) or of modified gravity (Milgrom 1983). For a more recent reviews on dark matter (DM) issues the reader can refer to Bertone & Tait (2018) and Amendola et al. (2018).

Basically, the absence of evidence of extra matter to justify the observed RC was the driving idea to state the need of DM also in the standard picture of structure formation in the early universe and in gravitational lensing due to the mass of galaxies (both model dependent and based on the chosen spacetime geometry). Given the

★ E-mail: mariateresa.crosta@inaf.it

purely gravitational nature of DM, recent search strategies look also for clues in strong-gravity regions or in gravitational wave signals generated by dynamically compact objects (Cardoso & Pani 2019).

Other alternatives focus on modifying the standard gravity theory, in particular the "geometric" part of the Einstein Equation, like $f(R)$ gravity (Buchdahl 1970; Starobinsky 1980; DeFelice & Tsujikawa 2010), where "dark" components can be avoided by varying the Ricci scalar. A wider class of theories, with higher-order curvature invariants and non-minimal couplings, extends the Einstein-Hilbert action of gravitational field to more actions (Fuji & Maeda 2004; Capozziello & De Laurentis 2011).

Recently, the non-extensive q-statistics[1] of the Boltzmann-Gibbs approach (Tsallis 1988; Tsallis & Arena 2014) has been applied in astronomy to describe the velocity distribution function of self gravitating collisionless particles on galactic scales. The RC flatness is considered in the context of Newtonian regime assuming a DM halo. Such a non-extensive distribution provides a way to describe DM cored haloes from first principles. For example, a set of polytropic, non-Gaussian, Lane–Emden spheres with the central value q = 0.85 yielded a successful fitting for all the observed RCs of some nearby spiral galaxies (Frigerio, Lima & Chimenti 2015, and references therein).

Most of these attempts are, however, based on unproved or *ad hoc* physical assumptions. Moreover, a common procedure is to consider the Newtonian limit of Einstein's equation, thus solving Poisson's equation in order to derive the velocities tracing the observed RC. Then the dynamics of galaxies is usually considered to be dominated by the Newtonian regime, and general relativistic effects included as corrections. In the linearized theory (i.e., an approximate version of Einstein's theory) and when the energy-momentum conservation reduces to $\partial_\beta T^{\alpha\beta} = 0$, the matter fields that produce $T^{\alpha\beta}$ are allowed to exchange energy and momentum between themselves but not with the gravitational field. As a consequence, the dynamics cannot include gravity and cannot be applied to gravitationally bound systems like stars, being dominated by non-gravitational forces (Poisson & Will 2014).

A few authors (Cooperstock & Tieu 2007; Balasin & Grumiller 2008) explored the weak relativistic regime of Einstein's equation for the galactic dynamics beyond the g_{00} term (and its corrections) or the spherical mass distribution. Almeida et al. (2016) compared both models to fit the rotation curves of some external galaxies.

Since our quest is pursuing a coherent general relativistic phase-space picture of the MW, it is worth reconsidering the level of "smallness" and, therefore, "negligibility" usually applied to Galactic dynamics, where the concept of *small velocity* is usually used since $v_{Gal}/c \approx 10^{-3}$ for typical Galactocentric rotational velocities of disk stars. According to the virial theorem, all forms of energy density within the gravitational bound system must not exceed the maximum value of its Newtonian potential. Regarding the measurements performed from within the weak relativistic regime of the Solar System (SS), the lowest order of contribution to the metric (e.g. the approximation of the term g_{00}) is $(v_{SS}/c)^2 \approx 2$ milli-arcsecond (mas), requiring the micro-arcsecond ray-tracing modeling for Gaia to include the non-diagonal term $g_{0i} \approx (v_{SS}/c)^3 \approx 0.2\mu$as. By applying the same reasoning to a conjectural metric for the Galaxy weak gravitational fields, the non-diagonal contribution is $\sim (v_{Gal}/c)^3 \approx 100$ μas, already within the error level of Gaia's DR2.

The small curvature limit in General Relativity (GR) may not coincide with the Newtonian regime, as it is the case of the Lense-Thirring effect (Lense & Thirring 1918). The situation appears similar to what was needed to explain the advancement of Mercury's perihelion: instead of correcting the dynamics by adding a "dark planet" (Vulcano), GR cured the anomalous precession by accounting for the weak non-linear gravitational fields overlapping nearby the Sun. Despite it amounts to only 43"/century, because of the small curvature, the effect was "strong" enough to justify a modification of the Newtonian theory. On the other hand, in the past it was fruitful to formulate new epistemological interpretations of accurate measurements, presenting new inexplicable features, possibly within the theory underlying them. The *aether*, for example, was removed by defining a new kinematics (i.e. the ansatz of special relativity, Einstein, 1905) that satisfied the Michelson-Morley experiment and Maxwell's equations, instead of adding a new dynamics, i.e. the "extra molecular force" from the Lorentz-FitzGerald contraction effect (Fitz Gerald 1889), to Newton's theory.

Currently, GR is the confirmed standard theory that explains gravity over a range of sixty orders of magnitude. We may certainly assert that the evolution of the MW, and its constituents, is the product of the action of gravity. This reason alone suggests to evaluate to what extent the Newtonian approximation of Einstein's field equation, i.e. the term g_{00}, should be the only one considered in describing the Galaxy dynamics or if other metric terms can concur to it. Nevertheless, only a few exact solutions of Einstein's equation exist, making it even the more difficult to detail a metric for the whole Galaxy, especially if it is made of different structures.

2 THEORETICAL MODELS FOR THE ROTATIONAL VELOCITY PROFILE

Given the premises above, our first attempt is to consider a simple relativistic model suitable to represent the Galactic disk as dust in equilibrium at a sufficiently large distance from a (rotating) central body[2] via stationary and axially-symmetric solutions for the disk metric. Also, the GR model is put in comparison with a classical MW rotation curve (MWC), comprising a bulge, a disk and a halo mostly made of DM.

2.1 Classical model for the MW rotation curve

For the bulge component of the MWC model, we consider Plummer's density profile (Pouliasis, Di Matte & Haywood 2017):

$$\rho_b(r) = \frac{3b_b^2 M_b}{4\pi(r^2 + b_b^2)^{5/2}}, \tag{1}$$

where, in cylindrical coordinates, the bulge spherical radius is $r = \sqrt{R^2 + z^2}$, with $b_b = 0.3$ kpc the Plummer radius (Pouliasis, Di Matte & Haywood 2017) and M_b the total bulge mass. As for the thin and thick MW disks, we use a double-component stellar disk modeled as two Miyamoto-Nagai potentials. This function is also approximated with a double exponential disk as in McMillan (2017) and Korol, Rossi & Barausse (2019). The most general description of a double-component MW disk (Bovy 2015; Barros, Lepine &

[1] q stands for the entropic-index quantifying the degree of non-extensivity in the entropic functional.

[2] This is the region above ~ 5 kpc populated by the Gaia stellar tracers (see section 3 below).

Dias 2016; Pouliasis, Di Matte & Haywood 2017) is expressed in the form

$$\rho_d(R,z) = \frac{M_d b_d^2}{4\pi} \frac{\left[a_d R^2 + \left(a_d + 3\sqrt{z^2+b_d^2}\right)\left(a_d + \sqrt{z^2+b_d^2}\right)^2\right]}{\left[R^2\left(a_d + \sqrt{z^2+b_d^2}\right)^2\right]^{5/2}\left(z^2+b_d^2\right)^{3/2}}, \tag{2}$$

where M_d is the total (thin or thick) disk mass, and a_d and b_d are scale–length and scale–height respectively. We set $b_{td} = 0.25$ kpc and $b_{Td} = 0.8$ kpc as the thin and thick disk scale-heights, following the work of Pouliasis, Di Matte & Haywood (2017) cited above.

Finally, for the MWC, we use a standard Navarro-Frank-White (NFW) model to describe the DM halo (Navarro et al. 1996; Bovy 2015; McMillan 2017) :

$$\rho_h(r) = \rho_0^{halo} \frac{1}{(r/A_h)(1+r/A_h)^2}, \tag{3}$$

where ρ_0^{halo} is the DM halo density scale and A_h its (spherical) scale radius.

The MW total potential is computed by solving the Poisson equation $\nabla^2\Phi_{tot} = 4\pi G(\rho_{bulge} + \rho_{td} + \rho_{Td} + \rho_{halo})$; then, the circular velocity follows by solving the differential equation $V_c^2(R) = R\,(d\Phi_{tot}/dR)$ (see subsection 3.3 for the actual derivation of the unknown parameters).

2.2 The general relativistic model

The same assumptions of the classical approach, namely that the masses inside a large portion of the Galaxy interact only gravitationally and reside far from the central bulge regions, can be made in GR assuming a pressure-less perfect fluid, i.e. GR dust, shear-free and expansion-free (Stephani et al. 2009), defined to be a continuous distribution of matter with stress-energy tensor $T^{\alpha\beta} = \rho u^\alpha u^\beta$ (in geometrized units). Here, the time-like vector field u^α represents the 4-velocity of the fluid proportional to a Killing vector $k^\alpha \propto \partial_0^\alpha$[3], while ρ is the mass density. Although a pressure-less fluid is not pure vacuum, it may be considered as a very close approximation to a low energy density regime (Wald 1984)[4]. Moreover the conservation equation implies geodesicity of the four-velocity and conservation of the mass-energy distribution.

As reported in Neugebauer & Meinel (1995) and Neugebauer, Kleinwächter & Meinel (1996), a rigidly rotating disk of dust is the universal limit of rigidly rotating perfect fluid configurations, where the ratio of pressure to energy density vanishes. Such a disk represents the simplest model of a self-gravitating rotating system with no interaction except gravitation, and it may serve as a crude model for galaxies with the stars considered as dust grains. The rigidly rotating disk of dust could generate an ergosphere similar to that around a Kerr black hole. At 5 kpc or more from the Galactic center, our stellar orbits are then far enough from such a central region, whose dimension are much less than 1 kpc (see Gravity collaboration 2018, for example), where very perturbed stellar motions (velocity of about of 10^4 km/s) should be considered instead.

As a matter of fact, in hydrodynamics, dust represents a many-particle system interacting via gravitational forces alone. In cosmology this exact solution is commonly used, i.e. FRLW metric for a dust fluid (Wald 1984). On the other hand, no similar global relativistic solution is known so far for the internal galactic dynamics, considering the Galaxy a rotating isolated matter distribution. This is due to the mathematical complexity of coupling the Vlasov equation, also called collisionless Boltzmann equations, with the Einstein field equation. Recently, some numerical schema has been proposed by Ames, Andréasson & Logg (2016, and references therein for further details).

If stars populating the disk can be retained isolated (stellar encounters become effective well below the parsec scale), the Galaxy can be considered globally isolated up to around 25 kpc, where flaring effects emerge, indicating the onset of external gravitational perturbations. At that scale the dust solution still represents a universal limit for the global dynamics, large enough to consider the rotation curve only due to the angular-momentum sustained stellar population, neglecting at first any possible intrinsic streaming motions or tidal forces.

The aforementioned considerations justify the following line element chosen by Balasin & Grumiller (2008, BG) to trace the velocity profiles of disk galaxies in a weakly relativistic scenario

$$ds^2 = -dt^2 + 2N d\phi dt + (r^2 - N^2)d\phi^2 + e^\nu(dr^2 + dz^2), \tag{4}$$

i.e. away from the central regions. As argued by these authors, the assumption of pressure-less perfect fluid simplifies the dynamics to be solved as compared to that in vacuum (Wald 1984).

In virtue of line element (A1) and conditions (A3), the unit tangent vector field of a general spatially circular orbit can be expressed as

$$u^\alpha = \Gamma\left(k^\alpha + \beta m^\alpha\right), \tag{5}$$

where β is the constant angular velocity (with respect to infinity) and Γ the normalization factor. Equation (5) represents a class of observers that includes static ones ($\beta = 0$), and can be parametrized either by β or equivalently by the linear velocity, say ζ, with respect to the ZAMOs (Z^α, Zero Angular Momentum Observers) as:

$$u^\alpha = \gamma\left(e_{\hat{0}}^\alpha + \zeta^{\hat{\phi}} e_{\hat{\phi}}^\alpha\right), \tag{6}$$

where $\gamma = -(u|Z)$[5] is the Lorentz factor, $e_{\hat{0}}^\alpha$ is the unit normal to the t=constant hypersurfaces, and $e_{\hat{\phi}}^\alpha$ the ϕ unit direction of the orthonormal frame adapted to the ZAMO.

ZAMO frames are, indeed, locally non-rotating observers, which have no angular momentum with respect to flat infinity and move on worldlines orthogonal to the hypersurfaces t=constant. The associated tetrad is: $e_{\hat{0}}^\alpha \equiv Z^\alpha$, $e_{\hat{\phi}}^\alpha \equiv 1/\sqrt{g_{\phi\phi}}\partial_\phi^\alpha$, and $e_{\hat{a}}^\alpha \equiv e^{-\nu}\partial_a^\alpha$.

Then, the line element (4) can be rewritten in terms of the lapse $M = r/\sqrt{(r^2 - N^2)}$ and the shift factor $M^\phi = N/(r^2 - N^2)$ as

$$ds^2 = -M^2dt^2 + (r^2 - N^2)\left(d\phi + M^\phi dt\right)^2 + e^\nu(dr^2 + dz^2), \tag{7}$$

where $Z^\alpha = (1/M)(\partial_t - M^\phi\partial_\phi)$ and the relationship between β and $\zeta^{\hat{\phi}}$ is given by equating equations (5) and (6)

$$\zeta^{\hat{\phi}} = \frac{\sqrt{g_{\phi\phi}}}{M}(\beta + M^\phi), \tag{8}$$

[3] Greek indices run from 0 to 3.

[4] It is worth underlining here that standard ΛCDM Cosmology is based on the Friedman-Lemaître-Robertson-Walker metric, namely a model valid for perfect fluid particles in a homogeneous and isotropic universe.

[5] Symbol (|) stands for the scalar product relative to the chosen metric.

which, in the case of a static observer, reduces to

$$\zeta^{\hat{\phi}} = \frac{N(r,z)}{r}. \tag{9}$$

Equation (9), then, represents the velocity of the co-rotating "dust particle" as measured by an asymptotic observer at rest with respect to the rotation axis and turns out to be proportional to the off-diagonal term $g_{0\phi}$ of the metric (4), i.e. the background geometry; therefore, it can be related to the relativistic gravitational dragging (de Felice & Clarke 1990). The same applies for a Kerr-like metric[6] where, with respect to a suitable tetrad, a static observer has a non-zero angular momentum with respect to infinity, i.e., $(\partial_\phi|u) = g_{0\phi}/\sqrt{-g_{00}}$ (de Felice & Clarke). On the other hand, ZAMOs have zero azimuthal angular momentum, i.e. $(\partial_\phi|Z) = 0$, but a non-zero angular velocity due to the gravitational dragging. Bear in mind also that the Gaia observables are developed with respect to the static observer $u^\alpha = (1/\sqrt{-g_{00}})\partial_0^\alpha$ locally at rest relative to the BCRS (in the gravitational fields of the Solar System), which reduces to be $\propto \partial_0^\alpha$ far away from it (Crosta et al. 2017). In general, any particle moving in a metric independent from t and ϕ coordinates has two conserved quantities, say, p_0 and p_ϕ. Consider to drop a particle "radially" from infinity with angular momentum $p_\phi = 0$; then, $p^\phi = g^{\phi 0}p_0$ and $p^0 = g^{00}p_0$. By taking $p^0 \propto dt/d\lambda$ and $p^\phi \propto d\phi/d\lambda$ (being λ an affine parameter) it results:

$$\frac{p^\phi}{p^0} = \frac{g^{\phi 0}}{g^{00}} = \frac{d\phi}{dt}, \tag{10}$$

namely, the particle acquires an angular velocity in the same direction of the rotating gravity source while approaching it (Padmanahan 2010).

The function $N(r,z)$ was constrained by Balasin & Grumiller (BG) to the separation anstaz $N(r,z) = R(r)F(z)$ and the reflection symmetry assumption. Their final expression is (eq. 25, Balasin & Grumiller 2008):

$$N(r,z) = V_0(R_{out} - r_{in}) + \frac{V_0}{2}\sum_{\pm}\left(\sqrt{(z \pm r_{in})^2 + r^2} - \sqrt{(z \pm R_{out})^2 + r^2}\right), \tag{11}$$

where the three parameters V_0, R_{out}, r_{in} were chosen, respectively, as the flat regime velocity, the extension of the MW disk and the bulge radius. Note that Balasin & Grumiller solve $N(r,z)$ by avoiding values that could prevent a physical solution, such as the localized exotic energy-momentum tensor attributed to Cooperstock & Tieu (2007, CT), or violate the weak energy condition and the assumption of vanishing pressure (see appendix B of Balasin & Grumiller, 2008 and references therein, for example Zingg, Aste & Trautmann, 2007). Such flaws still persist in the recent publications of Carrick & Cooperstock (2012) and Magalhaes & Cooperstock (2017), where the application of the CT model is extended to other galaxies including the Milky Way, and in addition the mass density profiles is estimated (see section 4 for further details). Cooperstock and Tieu also define the velocity as an approximation valid for $r \gg N$.

Both BG and CT models assume that $N(r,z)$ is separable and has reflection symmetry, which implies four solutions for $F(z)$. Cooperstock and Tieu use $F(z) = e^{-k|z|}$ (not smooth at z=0) and write the velocity as a linear superposition of Bessel functions of the first kind to get a good fit to the data. BG's model, instead, adopts $F(z) = \cos kz$, which leads to solutions involving modified Bessel functions and integrates over all possible modes to obtain expression (11).

Moreover, the metric of the BG model approaches the metric of flat space far from the centre of the Galaxy, whereas CT's solution for the metric approaches the flat space metric far from the galaxy in the azimuthal direction but not in the radial direction (Neill 2011). The BG model still lacks of an appropriate physical boundary for $r \ll N$ (Grumiller, Balasin & Preis 2008), the region where the metric is not defined in both models. In fact, as underlined also by the authors, the BG model has some limitations at $r = 0$ (where the motion becomes superluminal, the same in the classical Newtonian model) and $|z| > r_{in}$ (arbitrarily set to 1 kpc by BG). However, the rotation curve describes the velocity profile as a function of the radial coordinate only and the limitation on the z coordinate derives from the separability ansatz applied by BG to solve the metric function $N = N(r,z)$. This means that from RC data only, it is not possible to obtain a complete 3D description of the disk structure. In this context, if $|z|$ increases, the separability may be reconsidered taking into account the tilt of Local Velocity Ellipsoid (Everall et al 2019). Moreover, as the model implements a dust solution, the BG ansatz can affect the following aspects: i) the pressure-less condition can be broken in the central region, and ii) the older stellar populations, which mainly populate the MW thick disk, acquire a higher intrinsic scatter in the three velocity components. A more complex scenario should be considered in order to take into account perfect fluid solutions with non-vanishing pressure (Andreasson et al. 2011).

The considerations above might suggest a Galactic structure dominated, in the innermost part, by a Kerr-like source that, far away from it, turns into a perturbed Schwarzschild-like metric or a co-rotating "dust" (for example see Lynden-Bell, Katz & Bičák 1995).[7] All of the limitations might be overtaken by considering a global solution with appropriate metric conformal factors as well as suitable boundary conditions, which lead to a smooth transition from a Kerr-like metric to a stationary axially-symmetric solution for the disk-dominated regions. The spatial velocity profile can be defined via equation (8), and a valid mathematical solution should be found accordingly.

Equation (11), even though based on tailored assumptions, represents one of the first attempts at deriving a possible GR velocity profile, that is worth testing as an approximate case, before pushing for more reliable and complex solutions.

3 FIT OF GAIA-DR2 DATA TO CLASSICAL AND RELATIVISTIC MW ROTATION CURVES

In the following, we confront the models presented in the previous section for the MW rotation curves to the best data - that are independent from any model - we obtain only from the Gaia DR2. The model that would not fit these data should then be rejected.

3.1 Sample Selection

To study the RC profile of our Galaxy we selected stars tracing the MW disk from the recently released Gaia DR2 archive according

[6] The vacuum solution of the Einstein field equation for stationary, axisymmetric, asymptotically flat space-time.

[7] According to Stephani et al. (2009) there exists a one-to-one correspondence between static vacuum solution and (rigidly rotating) dust stationary solution (theorem 21.1).

to the following strict criteria: (i) availability of the complete astrometric set, and of its corresponding error (covariance) matrix (right ascension α and declination δ, the proper motions $\mu_\alpha \cos\delta$ and μ_δ, and parallax ϖ); (ii) availability of the Gaia-measured velocity along the line of sight, RV, and its error; (iii) parallaxes good to 20%, i.e., $\varpi/\sigma_\varpi \geq 5$; (iv) availability of a cross-matched entry in the 2MASS catalog (Skrutskie et al. 2006). Requirements (i) and (ii) are necessary for a proper 6-dimensional reconstruction of the phase-space location occupied by each individual star as derived by the same observer. As for the third criteria, parallaxes to better than 20% allow us to deal with similar (quasi–gaussian) statistics when transforming them into actual distances, as discussed in Smith & Eichhorn (2012) and references therein. Selection criteria (iv) is essential for the actual materialization of the sample of early type stars. In fact, it provides us with the 2MASS near-infrared magnitudes J, H, and K (Skrutskie et al. 2006) that, in combination with the G-band magnitude from the DR2, allow us to build the following photometric filter:

$$(J-H) < 0.14(G-K) + 0.02 \text{ and } (J-K) < 0.23(G-K)$$

Following Poggio et al. (2018), that needed a stellar sample tracing the MW disk for studying presence and possibly nature of its warp, this filter is then used in combination with their probabilistic method that uses Gaia's astrometry and photometry together to select stars whose colors and absolute magnitudes are consistent with them being upper main sequence stars, including OB stars (see also Re Fiorentin, Lattanzi & Spagna 2019). On the other hand, as mentioned above, Gaia-measured RV's made the DR2 catalogue only when the estimated stellar effective temperatures are between 3550 and 6900 K (Katz et al. 2019) for a total of $\sim$ 7.2 million objects. This implies that a large fraction, if not all, of the OB stars initially in the 2MASS cross-matched sample drops out of it because of the RV requirement (ii), leaving us with mainly A, and some F, early type stars. This contingent RV-induced bias will be greatly mitigated with the forthcoming Gaia deliveries.

Then, DR2 directly provided all of the data, i.e. astrometry (parallaxes and annual proper motions) and RVs, necessary for a proper 6-dimensional reconstruction of the phase-space location occupied by each individual star as derived by the same observer.

At the end of our selection process we are left with a very homogenous sample of 5277 early type stars and 325 classical type I Cepheides as classified by the Gaia pipelines (Clementini et al. 2019), the largest stellar sample of this kind ever.

3.2 Spatial and kinematical analysis

Both spatial and kinematical tests were conducted to ensure that the selected data set fairly traces the MW disk and its kinematics. A close look at the radial and vertical distributions of our sample shows that 99.4 % , (i.e. 5566) of its stars, are within $4.9 \leq r \leq 15.8$ kpc (a range of $\sim$ 11 kpc) and below 1 kpc from the galactic plane, that represents the characteristic scale height for the validity of the BG model.

The quantities extracted from the Gaia DR2 archive are transformed from their natural ICRS reference frame (Mignard et al. 2018) to its galactocentric cylindrical counterpart, i.e., into the quantities R, ϕ, and z for the galactocentric spatial coordinates and their corresponding velocities V_R, V_ϕ (i.e., the azimuthal velocity at any galactic longitude), and V_z.

The procedure followed is that described in the Gaia Data Release 1 (2017), and includes proper error propagation thanks to the availability of the correlation matrix (requirement (i)). For its actual application, we specified the values of the Sun's radial distance $R_\odot$ in the Galactic frame and the Sun's velocity $(U_\odot, V_\odot, W_\odot)$ directly in the Galacto-centric reference frame, as derived from the proper motion of Sgr A* (adopted as the Galactic center). In this way, we are independent from the local standard of rest. The following values were adopted after reviewing the recent literature: $R_\odot = 8.122 \pm 0.031$kpc (Gravity collaboration 2018) and $(U_\odot, V_\odot, W_\odot) = (12.9, 245.6, 7.78)$ km/s (Drimmel & Poggio 2018).

We then bin the data in cylindrical rings [R-ΔR, R+ΔR] as a function of R as described in the caption of Table 1.

Finally, we adopt RSE (from Robust Scatter Estimate) as a robust measure of the dispersion of a distribution. It is defined as $(2\sqrt{2}erf^{-1}(4/5))^{-1} \sim 0.390152$ times the difference between the 90th and 10th percentiles; RSE is the same as standard deviation in the case of a normal distribution. The values for $|z_{median}|$ and the median V_ϕ's are quite compatible with those expected for a population belonging to the MW young disk and confirm, in turn, the effectiveness of the procedure we adopted for extracting stars from the upper main sequence.

Moreover, the measured velocity dispersion in each radial bin, i.e. the intrinsic scatter that measures the "warmth" of a stellar population, is always below 41.4 km/s, with a typical (mean) value of 22.1 km/s, as expected for a young thin disk stellar sample. As a final robust and consistency check of our analysis, we calculate the circular(ized) velocity (Jeans 1915; Binney & Tremaine 2008) solving the cylindrical form of the Jeans equation for an axisymmetric disk, namely

$$\frac{\partial(\rho < V_R^2 >)}{\partial R} + \frac{\partial(\rho < V_R V_z >)}{\partial z} + \rho\left(\frac{< V_R^2 > - < V_\phi^2 > + V_c^2}{R}\right) = 0, \tag{12}$$

to circularize our V_ϕ. This equation links the moments of the velocity distribution $< V_i V_j >$ and the density ρ of a given stellar sample to the circularized velocity V_c. The circular(ized) velocity is then

$$V_c^2(R) = < V_\phi^2 > - < V_R^2 > \left(1 + \frac{\partial \ln \rho}{\partial \ln R} + \frac{\partial \ln < V_R^2 >}{\partial \ln R}\right), \tag{13}$$

where we neglected the contributions of the vertical gradients, and $< V_i^2 >$ represents the averaged squared velocity of the velocity matrix in each bin. Following Eilers et al. (2019), we utilized the exponential radial density profile $\rho(R) \propto exp(-R/h_r)$ with h_r = 3 kpc. Besides, we notice that in the radial range covered by our data ($\sim$ 5-16 kpc), the radial gradient of $< V_R^2 >$ (last term in the parenthesis of equation (13)) is close to zero. With equation (13) providing the measured values of V_c's in each radial bin, the corresponding uncertainties are computed via bootstrapping with 100 re-samples on the individual values of the azimuthal velocities. The total error takes also into account possible systematic errors (estimated within 5%) that the approximations mentioned above could introduce. There is a slight positive gradient towards larger radial distances, as naturally expected by Jeans' analysis. We verify that the corrections (due to the circularization procedure) to the observed azimuthal velocities are always well below 10% throughout the radial range we have probed (up to $\sim$ 10 km/s, i.e. below the intrinsic scatter of the population) and fairly consistent with the increasing uncertainties computed via the bootstrapping method.

Therefore, we decided to use the observed and *model-independent* azimuthal velocity profile to test the two models. This

bin_{size} (kpc)	R_{mean} (kpc)	$star_{count}$	z_{median} (kpc)	$V_{\phi,median}$ (km/s)	σ_{V_ϕ} (km/s)	RSE_{V_ϕ} (km/s)
0.2	5.0	3	-0.234	230	12	10.9
	5.2	7	-0.077	233	8	14.9
	5.4	13	-0.162	223	12	34.2
	5.6	14	-0.069	203	8	21.4
	5.8	30	-0.122	220	8	41.4
	6.0	40	-0.112	229	3	37.4
	6.2	71	-0.125	229	3	23.3
	6.4	102	-0.124	234	3	19.8
	6.6	156	-0.078	229	2	19.3
	6.8	244	-0.036	231	2	19.8
	7.0	273	-0.014	228	1	19.2
	7.2	364	0.007	229	1	20.2
	7.4	392	0.016	232	1	20.1
	7.6	428	0.023	233	1	18.7
	7.8	366	0.007	231	2	20.4
	8.0	368	0.010	234	1	19.7
	8.2	342	-0.010	231	2	20.9
	8.4	380	0.009	232	1	22.4
	8.6	368	-0.011	229	1	23.0
	8.8	343	-0.055	226	1	17.2
	9.0	296	-0.054	224	2	17.8
	9.2	219	-0.044	224	1	18.1
	9.4	202	-0.019	224	1	19.6
	9.6	155	-0.039	222	2	21.0
	9.8	105	-0.049	225	2	20.3
	10.0	77	-0.012	228	4	23.1
	10.2	51	0.007	219	6	32.9
	10.4	27	-0.067	230	2	21.1
	10.6	25	-0.032	234	5	22.5
	10.8	20	-0.031	230	6	32.3
	11.0	13	-0.103	232	8	15.0
0.4	11.3	19	-0.030	227	9	27.8
0.5	11.75	18	0.031	226	6	23.5
	12.25	20	0.061	229	14	21.3
	12.75	11	-0.039	227	5	18.8
	13.25	7	0.001	234	10	8.2
1	13.8	4	0.496	208	24	32.9
1.5	15.8	2	0.043	220	12	9.2

Table 1. Properties of the binned data for the stellar sample extracted from the Gaia DR2 archive. The data are grouped in cylindrical rings $[R - \Delta R, R + \Delta R]$ as a function of the cylindrical coordinate $r \equiv R$. Each radial bin is centered at the value shown in the second column. The bin size, ΔR, is 0.2 kpc except for the last bins that have been changed to cope with both increasing position errors with distance and the natural decrease in numbers of the Galaxy disk tracers. As robust estimates of the values representing each bin, medians and RSE's are used. The average of the median distances from the plane is $< z_{median} >$= -0.027 kpc in the range between Max(z_{median})= 0.496 kpc and Min(z_{median})=-0.234 kpc; moreover, the average value for the vertical dispersion is 0.206 kpc. As for the azimuthal velocity V_ϕ, the weighted average (across the bins) of the median V_ϕ is $\sim$ 224 km/s, while the measured intrinsic velocity dispersions are always below 41.4 km/s, with a typical (mean) value of 21.1 km/s, and always larger than the uncertainties on the median value σ_{V_ϕ}.

preserves the internal consistency of our work, since the Jeans analysis assumes Newtonian gravity and not a complete relativistic description. To our knowledge, a possible relativistic Jeans' analysis could be done numerically (Ames, Andréasson & Logg 2016) or with a post-Newtonian approximation (Nazari et al. 2017). Nevertheless, the implementation of the Jeans correction has no significant effect as all of the results are compatible in the statistically credible interval of the posteriors (as reported in appendix C, tables C1, C2, C3, and C4).

As already mentioned, we selected the most suitable stellar sample to ensure the effective applicability of a pressure-less perfect fluid model to the Galaxy. As further proof of this hypothesis, note that in Table 1 the intrinsic velocity dispersion, equivalent to a pressure term in the Jeans equation, is on average less than 10% compared to the azimuthal speed in each bin.

3.3 The fits to relativistic and classical MW rotation curves

In the equatorial plane, after setting $r \equiv R$ and $V^{BG}(R) \equiv \zeta^{\phi}(r)$ in equations (9) and (11), the relativistic velocity profile writes:

$$V^{BG}(R) = \frac{V_0}{R}\left(R_{out} - r_{in} + \sqrt{r_{in}^2 + R^2} - \sqrt{R_{out}^2 + R^2}\right), \qquad (14)$$

where the unknown parameters V_0, R_{out}, r_{in} will result from fitting to the data of Table 1 after transforming from geometrized back to

BG model	θ	σ_θ^-	σ_θ^+
r_{in} [kpc]	0.39	-0.25	+0.36
R_{out} [kpc]	47.87	-14.80	+23.96
V_0 [km/s]	263.10	-16.44	+25.93
e^{ν_0}	0.083	- 0.014	+0.014

Table 2. r_{in}, R_{out} and V_0 are the parameters of BG's model that correspond, respectively, to the lower and upper radial limits, i.e. the bulge radial size and the Galaxy radius, and the normalization of the velocity in the flat regime. e^{ν_0} is the estimated dimensionless value characterizing the conformal factor function, assumed constant, in line element (4). θ, σ_θ^- and σ_θ^+ are the mean and the 1σ credible interval limits from the posteriors of the parameters (see also the values in Table C1 of appendix C, to which this table is fully compliant).

MWC model	θ	σ_θ^-	σ_θ^+
$M_b[10^{10}\mathrm{M}_\odot]$	1.0	-0.4	+0.4
$M_{td}[10^{10}\mathrm{M}_\odot]$	3.9	-0.4	+0.4
$M_{Td}[10^{10}\mathrm{M}_\odot]$	4.0	-0.5	+0.5
a_{td}[kpc]	5.2	-0.5	+0.5
a_{Td}[kpc]	2.7	-0.4	+0.4
$\rho_0^{halo}[\mathrm{M}_\odot\mathrm{pc}^{-3}]$	0.009	-0.003	+0.004
A_h [kpc]	17	-3	+4

Table 3. $M_b, M_{td}, M_{Td}, a_{td}, a_{Td}, \rho_0^{halo}$ and A_h are the free parameters of the MWC model: the bulge mass, the masses and the scale lengths of the two disks, the halo scale density, and the halo radial scale, respectively. θ, σ_θ^- and σ_θ^+ are the mean and the 1σ credible interval limits from the posteriors of the parameters (see also the values in Table C3 of appendix C, to which this table is fully compliant).

regular units. In other words, these quantities identify the range for which the 4D spacetime metric used can describe the MW disk as an axisymmetric stationary rotating dust.

This relativistic velocity profile is then compared to the well-studied classical models for the MW described in section 2. Each contribution to the azimuthal (circular) velocity in the classical model is calculated by utilizing the *GALPY* python package (Bovy 2015).

We fit both the BG and MWC models to the DR2 azimuthal velocity data $V_\phi(R_i)$, and the corresponding uncertainties, from Table 1, utilizing the log likelihood function

$$\log\mathcal{L} = -\frac{1}{2}\sum_i\left(\frac{[V_\phi(R_i)-V_\phi^{exp}(R_i|\theta)]^2}{\sigma^2_{V_\phi}}+\log\left(\sigma^2_{V_\phi}\right)\right) - \frac{1}{2}\left(\frac{[\rho(R_\odot)-\rho^{exp}(R_\odot|\theta)]^2}{\sigma^2_{\rho_\odot}}+\log\left(\sigma^2_{\rho_\odot}\right)\right), \quad (15)$$

where $V_\phi^{exp}(R_i|\theta)$ are the expected velocity values evaluated with the two theoretical models at each R_i for any trial set of their corresponding parameter vector θ.

For the "observed" (local) baryonic matter density at the Sun and its corresponding error, i.e. $\rho(R_\odot)$ and $\sigma_\odot$, in the likelihood function above, we adopted the most recent values, respectively 0.084 and 0.012 $\mathrm{M}_\odot\mathrm{pc}^{-3}$, given in McKee, Parravano & Hollenbach (2015).

For the BG model (Balasin & Grumiller 2008), $\rho^{exp}(R_\odot|\theta)$ at z=0 is calculated via the 00-term of Einstein's equation (see section 4), while for the MWC model $\rho^{exp}(R_\odot|\theta) = \rho_b(R=R_\odot, z=0) + \rho_{td}(R=R_\odot, z=0) + \rho_{Td}(R=R_\odot, z=0)$ from equations (1) and (2).

In summary, we decided for 7 free parameters when fitting with the MWC model, i.e. M_b, M_{td}, M_{Td}, a_{td}, a_{Td} ρ_0^{halo} and A_h. Instead, when dealing with the BG model, we have a total of 4 free parameters, V_0, R_{out}, r_{in} and e^{ν_0} (see section 4), and contrary to the MWC case, the use of the BG density function ρ^{BG} in the likelihood expression above is mandatory, as e^{ν_0} is not present in $V^{BG}(R)$.

We finally used the Markov-Chain Monte-Carlo (MCMC) method to fit to the data (see appendix B); Tables 2 and 3 report the best fit estimates as the median of the posteriors and their 1σ level credible interval. For both models, the errors due to the Bayesian analyses are at least one order of magnitude lower than the resulting uncertainties of the parameters. This shows that the analysis is intrinsically consistent and the simulation errors are negligible.

In Figure 1, the star-like symbols show median V_ϕ versus R as derived with the Gaia DR2 data in Table 1. The two MCMC estimated velocity profiles, drawn as the coloured solid lines in Fig. 1, are both good representations of the data , i.e., they are statistically equivalent (see appendix C).

The least constrained parameter in the BG model is the "upper" radial limit, i.e., R_{out}. As already discussed, this was actually expected due to a relatively limited radial coverage of the Gaia-only velocity data we have used. Besides, we obtain an interesting result on the lower limit parameter r_{in}. According to Balasin & Grumiller (2008, after their Eq. 26), as r_{in} "determines the transition between the linear ($r \ll r_{in}$) and the flat ($r_{in} \ll r \ll R_{out}$) regime of the velocity profile", the size of the bulge " may be predicted from the velocity profile". Remarkably, the fitted value r_{in} = 0.39 kpc in Table 2 is quite close to the value of b_b = 0.3 kpc we adopted from Pouliasis et al. (2017; see also Eilers et al, 2019) for the Plummer's radius of the bulge contribution to the MW density in our MWC model (see Eq. 1 in sec. 2.1). It is also important to highlight here the back-compatibility of this experimental result with the z distribution of our selected disk population (see Table 1 and its caption): to ensure a consistent application of the BG velocity model, the selected stars resulted in a population spatially constrained to small distances from the plane (average median height $< z_{median} > \approx$ -0.03 kpc and a corresponding average dispersion of 0.2 kpc), and, in turn,$< z_{median} > \leq r_{in}$ virtually everywhere across the radial range spanned by the Gaia rotational velocity data. Despite this ability of providing an independent measurements of the radial size of the MW bulge directly from the velocity data, the existence of the critical regions at $|z| > 0.39$ kpc limits the physical validity of the BG model and prevents it from describing large parts of the actual Galaxy.

It is worth mentioning that Almeida et al. (2016) converted the observational RC's for some external galaxies into a data set of an effective analogue (called the "effective Newtonian" velocity profile V_{eN}) in order to define a method to compare non-Newtonian gravity models with or without some dark matter. From the fit of the Newtonian velocity profile to the effective Newtonian curve the authors derive some baryonic parameters (basically by solving Poisson-like equations). With the application of such a method, it appears that both CT and BG approaches have strong problems fitting galaxy rotation curves without dark matter. On the other end, the statistical technique used for the fit, i.e. a χ^2 minimization procedure, could be insufficient for exploring the parameter space (see appendix B) and some parameters appear not suitable for a consistent representation of the BG model. For example, the galaxy radius $R \sim 10^7$ kpc is out of the range given by the BG solution and galaxies cannot be considered isolated at such distances. Despite

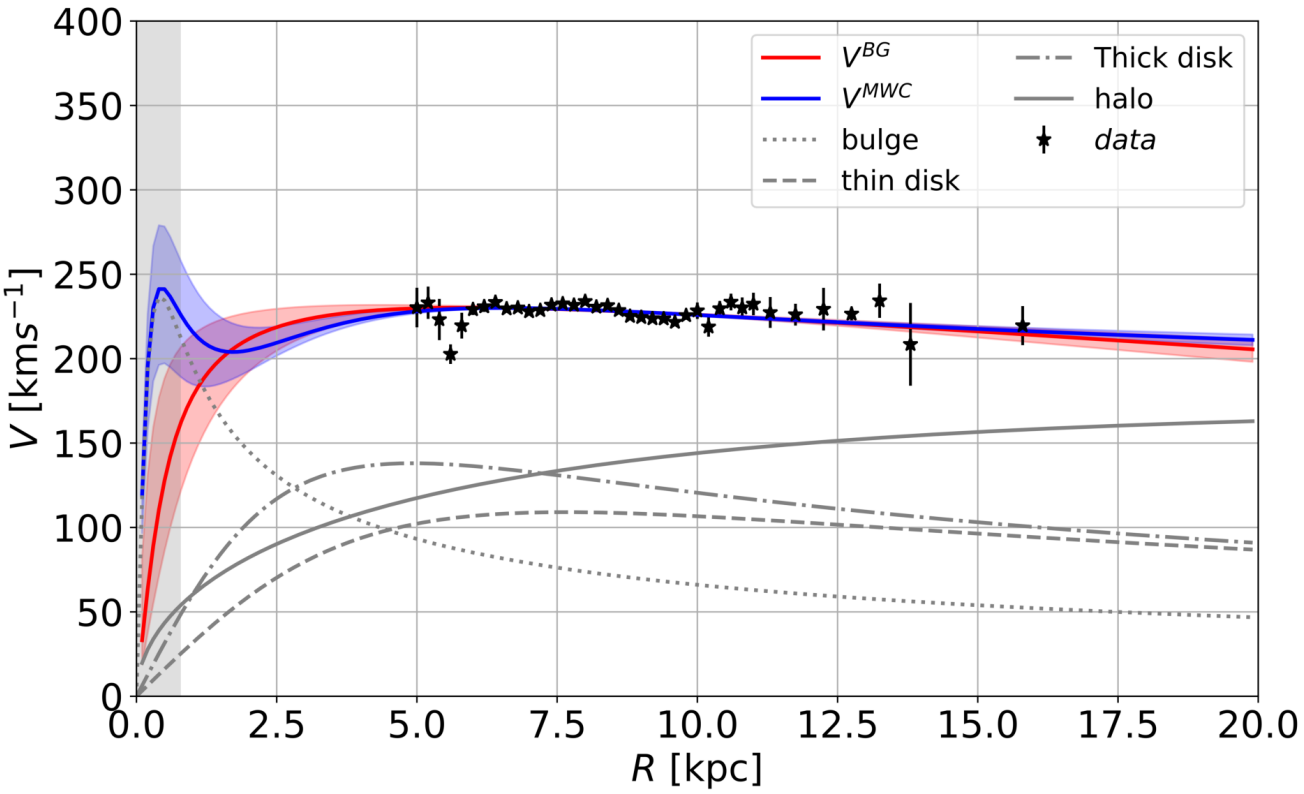

Figure 1. The azimuthal velocity profile of the MW as derived from the sample of disk tracers selected from the Gaia DR2. The black starred symbols represent the median values within each of the radial bins in Table 1. The corresponding error bars are computed via bootstrapping (see text). The red and blue curves show the best fit to the BG and MWC models, respectively. The other grey curves represent the kinematical substructures that contribute to the MWC model: the dotted line is for the bulge, dashed and dot-dashed lines are for thin and thick disk, respectively. Finally, the grey solid line illustrates the contribution of the NFW halo. The coloured areas represent the reliability intervals of the fitted curves; note that for $R < 5$ kpc both the classical and the relativistic curves are very uncertain because of the lack of data in that region. The grey vertical band represents twice the value of r_{in} estimated with the BG model.

that, the fact that BG or CT densities do not fit V_{eN} in the absence of DM indicates that off-diagonal terms, not analyzed in Almeida et al. (2016), might account for the contribution that flattens the observed rotation curves.

4 THE MASS DENSITY

In the case of the metric function adopted for the BG model, the 00-term of Einstein's field equation results (for its derivation see appendix D):

$$\rho^{BG}(R,z) = \frac{(\partial_R N(R,z))^2 + (\partial_z N(R,z))^2}{8G\pi R^2 e^{\nu(R,z)}}, \tag{16}$$

where $\rho^{BG}(R,z)$ is the mass density at (R,z) and $e^{\nu(R,z)}$ is the dimensionless conformal metric factor defined in equation (7). It is suggestive to note that for $R \to \infty$ and $z \to \infty$ the density approaches zero (Neill 2011), however we warned in the previous section on the inadequacy of the BG model to represent our Galaxy for regions above $|z| = r_{in} = 0.39$ kpc. Finally, with R and z in kpc, the estimated model parameters as in Table 2, and $G = 4.3 \cdot 10^{-6}$ kpc km^{2}sec^{-2}M$_\odot^{-1}$, Eq.(16) yields the density in M$_\odot$pc^{-3}.

4.1 The relativistic mass density at $R_\odot$

With the values in Table 2 inserted in Eq. (16), we obtain, for the local baryonic matter density, $\rho(R = R_\odot, z = 0) \equiv \rho_\odot = 0.083 \pm 0.006$ M$_\odot$pc^{-3} that is in agreement with independent current estimates, like, e.g., the estimate of $0.098^{+0.006}_{-0.014}$ M$_\odot$pc^{-3} in Garbari et al. (2012), the 0.077 ± 0.007 M$_\odot$pc^{-3} value of Bienayme et al. (2014), and the most recent determination of 0.084 ± 0.012 M$_\odot$pc^{-3} by McKee, Parravano & Hollenbach (2015), the local mass density used as the observed datum in the likelihood function of Eq.(15).

Notice that the value of the local baryonic matter density just derived with the BG model is truly the result of a fitting procedure with the (crude) assumption that the conformal metric factor is constant with R, i.e., $e^{\nu(R,z=0)} \approx e^{\nu_0}$. This procedure is different from that of Balasin & Grumiller (2008). Instead of a priori approximating e^{ν} (see sections 3.2 and 3.3 of Balasin and Grumiller) to compare the mass density (16) to the Newtonian regime, we assume a functional behaviour for the conformal factor and use this in the expression of ρ^{exp} utilized in the likelihood function (15). Of course, with just one reliable observed density value at our disposal, i.e. that at $R = R_\odot$, we are somewhat "forced" to consider a constant e^{ν} [8] leading to the dimensionless estimation of $e^{\nu_0} = 0.083$ in Table

[8] A similar approach was used by Magalhaes & Cooperstock (2017) in

2. Then, it is worth recalling here that, as explained in appendix B, the MCMC fitting procedure allowed e^{ν_0} to vary freely (i.e. uniformly distributed, as for the rest of the BG model parameters) in the interval [0.001, 10], a four orders-of-magnitude range.

This situation is much different from Newtonian dynamics (see McMillan 2017; Pouliasis, Di Matte & Haywood 2017; Eilers et al. 2019), where the rotational velocity data alone suffice to fit all of the parameters needed to define the different contributions to the Galaxy density functions via the relations (1), (2) and (3). Instead, the density in the BG relativistic model can be estimated only through its direct use in the likelihood function (15). Therefore, if more direct baryonic mass density measurements were available throughout the plane, our method could be used to determine a more general function for the density, i.e. for the conformal metric factor near the plane, $e^{\nu(R,z\sim0)}$, and verify, in turn, the overall consistency of the GR model or test more general ones, as they become available. So far, despite the tremendous improvement brought about by the Gaia DR2, we still do not have a suitable survey with the appropriate completeness due to systematic biases and observational limitations (Gaia Collaboration 2018; McKee, Parravano & Hollenbach 2015). The evaluation of the observed density profile from independent data, for example mass luminosity ratios, is beyond the scope of this work, but future implementations with the forthcoming new deliveries of the Gaia data might help in extending our results, especially from R ~ 5 kpc inward.

4.2 The mass density in the galactic plane

When evaluated at $z = 0$, the term $\partial_z N(r,z)$ in Eq. (16) goes to zero everywhere; then, Figure 2 compares the density profiles in the galactic plane of both the BG and MWC models once the best-fit values in Table 2 and Table 3 are utilized, respectively.

Looking at the results on our MWC model, comprising baryonic and DM density profiles, these are quite compatible with what shown in McMillan (2017), Pouliasis, Di Matte & Haywood (2017), and Eilers et al. (2019). This confirms the goodness of the "classical" part of our analysis and provides a baryonic mass density profile via the usual kinematic approach. In more detail, as expected in the disk region ($z \sim 0$), the dominant matter is baryonic, $\rho_{bar} \sim 0.08 - 0.10\,\mathrm{M_\odot pc^{-3}}$ at $R_\odot$, while DM is a minor component there, i.e. $\rho_{\mathrm{DM}} \sim 0.01\mathrm{M_\odot pc^{-3}}$, because of their different spatial distribution. Indeed, while stars and gas (as baryonic matter) are mainly concentrated close to the galactic disk, DM is distributed in a far larger spherical volume surrounding the Galaxy, i.e. the DM halo. Consequently, DM is much more "diluted" near the plane. Nonetheless, the total amount of DM is higher than ordinary matter also in our MWC model, as our analysis estimates that within a spherical volume of $R = 30$ kpc the baryonic mass (bulge, thin and thick disk) totals $\mathrm{M}_{bar} = 6.8 \cdot 10^{10}\,\mathrm{M_\odot}$, while the DM halo has a virial mass of $\mathrm{M_{DM}} = 1.09 \cdot 10^{12}\,\mathrm{M_\odot}$. Similarly, McMillan (2017) found a total stellar mass of $(5.43 \pm 0.57) \cdot 10^{10}\,\mathrm{M_\odot}$ and a total virial mass (composed mainly of DM) of $(1.30 \pm 0.30) \cdot 10^{12}\,\mathrm{M_\odot}$. Note also that the value obtained by Magalhaes & Cooperstock (2017) for the MW is $9.3 \cdot 10^{10}\,\mathrm{M_\odot}$.

Given the above, Figure 2 shows that the baryonic MWC profile and its BG analogue (the two solid lines) are almost coincident in the radial range above ~ 4 kpc. The two models predict a very similar baryonic mass distribution in the Galactic disk (at $z = 0$ kpc) in the radial range, $5\,\mathrm{kpc} \leq R \leq 16\,\mathrm{kpc}$, explored by the Gaia data. Furthermore, our fit procedure confirms that in that same distance range the assumption of a constant value for e^ν holds.

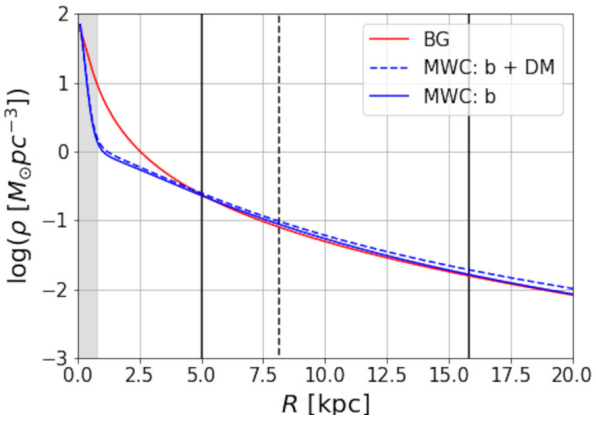

Figure 2. The density profile of the MW at $z = 0$ derived from 100 random draws from the posterior distribution of the fit. As in Figure 1, the red solid line is the BG model, while the blue dashed line represents the total matter contribution for the MWC model (i.e. the sum of the bulge and the two disks as the baryonic counterpart, plus the dark matter halo). The blue solid line shows the contribution of the sole baryonic matter. The vertical black solid lines limit the range of our data, while the vertical black dashed line indicates the Sun position in the Galaxy. Finally, the grey vertical band represents twice the value of r_{in} estimated with the BG model.

Figure 2 also shows that, differently from before, for $R \leq 4$ kpc (inside the MW bulge regions) the BG mass density profile in the plane, assumed of baryonic nature, demands more mass than what provided by the density components, dark halo included, of the MWC model (e.g., 10 times more at $R \sim 0.8$ kpc). Therefore, the question arises if the amount of actual baryonic mass within 4 kpc predicted by the two models is compatible or not. For our MWC model, we integrated the three baryonic components of our best fit densities in the region [$R \leq 4$ kpc; $|z| \leq 10$ kpc] for the two disks (10 kpc is more than 10 times the scale-height adopted for the thick disk), and within the spherical region $r \leq 4$ kpc of our Plummer bulge (4 kpc is more than 10 times the b_b value used for the bulge radius). The integration yields a MWC baryonic mass of $3.5 \cdot 10^{10}\,\mathrm{M_\odot}$, value that compares quite favorably with the $4.8 \cdot 10^{10}\,\mathrm{M_\odot}$ derived from integrating the BG mass density in the region $\epsilon \ll R \leq 4$ kpc, with $\epsilon \ll 1$ kpc [9], and $|z| \leq |z|_{eff} = 0.215$ kpc. Here, $|z|_{eff}$ represents the effective half-thickness of the BG MW disk, and its value is, as it should (see the previous section and the beginning of this), below r_{in}; as for its derivation, we defer it to the following section.

choosing the best fit for the Galaxy RC with the CT model, although $e^\nu = 1$ in their model.

[9] The Mathematica (2012) script we have written to deal with these calculations provides an extremely small estimate for ϵ when $|z| \leq r_{in}$, confirming that the radial extent of the region where the BG model is not defined is very close to the z-axis. It is only when $|z|$ increases above 0.39 kpc that the radial upper limit of the forbidden region, i.e. where $R < N(R,z)$ (see sec. 2.2), starts deviating significantly from R=0.

5 GRAVITATIONAL DRAGGING AND DARK HALO CONTRIBUTIONS TO THE MILKY WAY ROTATION CURVE

Following Almeida et al. (2016), we used the relativistic density ρ^{BG} (Eq. 16), for calculating the effective Newtonian circular velocity profile V_{eN}^{BG} at any given point along R from the relation of Binney & Tremaine (2008, see equation (16), sec. 3.2 of Almeida et al.). Of course, the extension of the integration along the direction perpendicular to the Galactic plane in the formula for $(V_{eN}^{BG})^2$ must be restricted to the region $|z| \leq r_{in}$= 0.39 kpc. With this definition of V_{eN}^{BG}, we are able to evaluate the amount of rotational velocity at $z = 0, V_{drag}^{BG}$, due to gravitational dragging, which has no Newtonian counterpart, and then compare it with the DM contribution to V^{MWC}.

The method adopted unfolds as follows. Let us define the square differences $(V_{eN}^{BG}(R_i; k) - V_{eN}^{MWC}(R_i))^2$ between the relativistic effective Newtonian rotational velocity at R_i and its pure Newtonian analogue, $V_{eN}^{MWC}(R_i)$; this is readily calculated as $V_{eN}^{MWC} = \sqrt{V_{bulge}^2 + V_{td}^2 + V_{Td}^2}$, where V_{bulge}, V_{td} and V_{Td} are the circular velocities due to the MW bulge, thin and thick disk, respectively (the broken line curves depicted in Figure 1). Next, we build the quadratic form $(\Sigma_i(V_{eN}^{BG}(R_i; k) - V_{eN}^{MWC}(R_i))^2)/N$, where N is the total number of R_i's we decide to utilize in the radial domain of our experimental velocity data (i.e., $R \geq 5$ kpc), having placed them ΔR_{step} kpc apart from R_1= 5 kpc to $R_N = ((N-1) \cdot \Delta R_{step} + 5)$ kpc (up to 20 kpc). The second index k identifies the half-thickness $|z|_k \leq r_{in}$, of the k-th BG disk we use in the vertical integral of the formula for the effective Newtonian circular velocity to compute numerically each $V_{eN}^{BG}(R_i; k)$ value, as the index i runs from 1 to N. The intention is now clear, we try to make the two effective Newtonian velocity profiles as similar as possible, in the radial range explored by Gaia, by minimizing the quadratic form above as function of the relativistic disk half-thickness $|z|_k = k \cdot z_{step}$, with k = 1, ..., M and $|z|_M \leq r_{in}$. For the effective BG disk half-thickness $|z|_{eff}$, the minimization process yields $|z|_{eff}$ = 0.215 kpc, for ΔR_{step} = 0.1 kpc and z_{step} = 0.005 kpc. Smaller radial and/or vertical steps changes only the non-significant digits of the $|z|_{eff}$ value. Also, notice that, as $|z|_k$ increases to the physical limit of 0.39 kpc, the BG effective Newtonian circular velocities grow to unrealistic rotational velocities, well above the $V^{BG}(R)$ profile itself, for ever larger portions of the Galactic plane. Actually, for $|z|$=0.39 kpc $V_{drag}^{BG}(R)$ is already unrealistically higher than the $V^{BG}(R)$ curve throughout the whole radial interval shown in Figure 3. The red solid curve in Figure 3 illustrates the $V_{eN}^{BG}(R; |z|_{eff})$ that the minimization finds closest to $V_{eN}^{MWC}(R)$, the blue solid line in the picture. Then, we are finally able to calculate the amount of rotational velocity across the MW plane due to gravitational dragging: this is done by simply taking the square root of the quadratic difference between the BG velocity profile, Eq. (14), and the effective Newtonian circular velocity, as computed above, for the disk half-thickness $|z|_{eff}$, i.e., $V_{drag}^{BG}(R; |z|_{eff}) = \sqrt{(V^{BG}(R))^2 - (V_{eN}^{BG}(R; |z|_{eff}))^2}$. The $V_{drag}^{BG}(R; |z|_{eff})$ profile is shown in Figure 3 by the red dashed line and is compared to the blue dashed curve $V_{\rm DM}^{MWC}$, the contribution of the DM halo to $V^{MWC}(R)$ (this is the same as the grey continuous line in Fig. 1). The gravitational dragging curve nears zero at R ~4.5 kpc, where $V_{eN}^{BG}(R; |z|_{eff}) \sim V^{BG}(R)$, then grows sharply within 2.5 kpc outwards to resemble the DM curve for most of the range to R = 20 kpc. This shows quantitatively that gravitational dragging can plausibly compensate for the need of a dark halo to sustain the flat velocity profile at large radii from the Galactic center as long as $|z|_{eff}$= 0.215 kpc is used in the context of the BG model.

For $R \leq 5$ kpc (the region we cannot constrain with the Gaia data at the moment), the two effective Newtonian velocities differ sharply, to the point that, for R below ~ 4.5 kpc, $V_{eN}^{BG}(R)$ grows unrealistically above $V^{BG}(R)$ itself. Possibly, this is signaling the limit of the applicability of the effective Newtonian velocity in combination with a density model, ρ^{BG}, unsuited, with just a disk component, to represent the complex structure of the MW especially toward its central regions.

This could be the breaking point for the direct applicability of the BG model to the Milky Way, as it calls for a more suitable relativistic description of its central regions. This would require to abandon the separability ansatz, as well as to find a more general solution for $e^{\nu}(R, z)$. Despite these limitations, the consequence of the application of an axisymmetric stationary metric, i.e. the ansatz solution for $N(R, z)$, to Einstein's equations (red line in Figures 2 and 3) is already rather significant. This points to the possibility that a gravitational dragging-like effect could sustain a flat RC. Obviously, more data and much improved mathematical models are necessary before such a scenario can be confirmed.

6 FINAL REMARKS

What we wish to emphasize first in this final section is that, for the classical DM model form adopted, we obtain results really in line with the most recent derivations from fits to data and samples different from the Gaia material used in this work.

Here, utilizing the same highly accurate Gaia data, we report also on our analysis with a simple GR model - a first order approximations to the Galaxy dynamics - as it has received much less attention over the recent years, thus providing a first test of its applicability to the MW rotation curve along the line pursued by (Almeida et al. 2016) with data on external galaxies.

The totality of observational clues of DM point to the existence of a material that: first, does not absorb or emit light but it exerts and responds only to the gravity force; second, enters the calculations as extra mass required to justify the flat galactic rotational curves. The proved relativistic ansatz, by accounting for a gravitational dragging effect driving the Galactic RC, could imply that geometry - unseen but perceived as manifestation of gravity according to Einstein's equation - might be responsible of the flatness at large Galactic radii. Then, there would be nothing new in saying that GR is the standard theory of gravity: our results seem to confirm this manifestation by accounting, via the Einstein field equations, for a "DM-like" effect. These equations link the source to the geometry of spacetime, and the proved ansatz suggests that their application to more physically appropriate metrics, along with adequate solutions, may yield an explanation to the RC flatness problem in our Galaxy.

Pursuing a GR picture of the MW can ensure a coherent Local Cosmology laboratory, i.e. at zero redshift, against which any model of the Galaxy can be tested; then the Galaxy can play a reference role, much like the Sun for stellar models. While Gaia offers a unique opportunity to trace star by star the Galactic potential from within the Solar System gravitational fields, by setting a coherent GR framework, one can effectively establish to what extent can GR account for DM. Our outcomes seem to suggest that global MW dynamics could be dominated by spacetime, whereas Newtonian approximation is valid only locally. Future developments of the

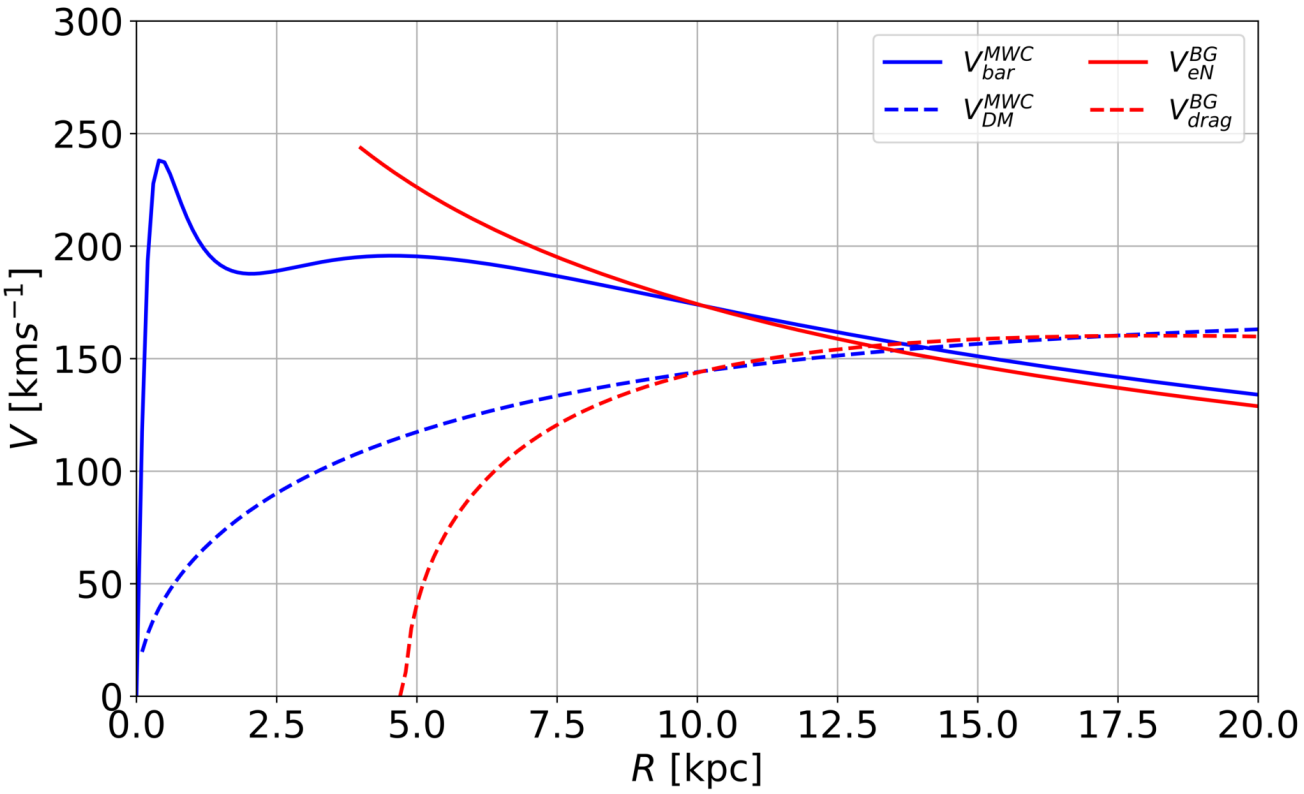

Figure 3. Red and blue colors refer to the BG and MWC model, respectively. Solid lines represent the relativistic effective Newtonian rotation curve, V^{BG}_{eN}, and its analogue for the MWC model, as contributed by the total of baryonic mass. The dashed lines show the MWC halo component alone, and the gravitational dragging contribution to V^{BG}, V^{BG}_{drag}, obtained by subtracting V^{BG}_{eN} from V^{BG} itself (see sec. 5 for details).

present work, theoretical and observational (with Gaia DR3 for example), might confirm this scenario.

As far as our ansatz is concerned, it appears that GR dust, namely pure matter made only of the non-collisional baryonic material in the disk, recovers the local energy-mass density, without further hypothesis (as per Occam's razor rule), within the 11-kpc range covered by our selection of disk stars from Gaia's DR2.

Although these are initial results based on a tailored physical solution of the Einstein field equation, they indicate a possible GR approach to the RC flatness problem in the spirit of the Newtonian *Hypotheses non fingo*, suggesting at the same time to push on the use of General Relativity, regardless of how difficult this might be, to detail a more complex Galaxy structure, mostly shaped by the bulky central rotating mass-source, where dragging effects could be further enhanced by similar sources distributed along the disk (see, for example, Liu J. et al. 2019).

ACKNOWLEDGEMENTS

This work has made use of data products from: the ESA Gaia mission (gea.esac.esa.int/archive/), funded by national institutions participating in the Gaia Multilateral Agreement; and the Two Micron All Sky Survey (2MASS,www.ipac.caltech.edu/2mass).

We are indebted to the Italian Space Agency (ASI) for their continuing support through contract 2014-025-R.1.2015 to INAF. We are grateful to and acknowledge the work of the Referee, whose valuable comments and suggestions improved our work. We thank Nezihe Uzun and David L. Wiltshire for having forwarded us the project report of Cathy Neill. We also acknowledge Marco Bruni, Paola Re Fiorentin, Ronald Drimmel, and Alessandro Spagna for fruitful discussions on computational schemas and selection of stellar samples.

REFERENCES

de Almeida A.O.F. et al., 2016, MNRAS, 462, Issue 3
Amendola L. et al., 2018, Living Rev. in Relativ., 21:2
Ames E., Andréasson H., Logg A., 2016, Class Quantum Grav., 33, 155008
Andréasson, H. et al., 2011, Living Reviews in Relativity, 14: 4
Balasin H., Grumiller D., 2008, Int. J. of Mod. Phys. D, 17, 475
Barros D. A., Lepine J. R. D., Dias W. S., 2016, A&A, 593, A108
Bertone G., Tait T. M. P., 2018, Nature, 562, 51- 56
Binney J., Tremaine S. 2008, Galactic Dynamics. Princeton Univ. Press, Princeton, NJ
Bienaymé O. et al., 2014, A&A, 571, A92
Bovy J., 2015, ApJs, 216, 29
Buchdahl H. A., 1970, MNRAS, 150, 1
Cardoso V. , Pani P., 2019, Living Rev. Relativ., 22: 4
Carrick J.D., Cooperstock F.I., 2012, Astrophys. Space Sci., 337, 321
Capozziello S., De Laurentis M., 2011, M. Phys. Rept., 509, 167
Clementini G. et al., 2019, A&A, 622, A60
Crosta M., Geralico A., Lattanzi M. G., Vecchiato A., 2017, Phys.Rev.D, 96,104030
Cooperstock F. I., Tieu S., 2007, Int. J. of Mod. Phys. A, 22, 13, 2293-2325

de Felice F., Clarke J. S., 1990, Relativity on curved manifolds. Cambridge University Press, Cambridge, UK
De Felice A., Tsujikawa S., 2010, Living Rev. in Relativ., 13
Fuji K., Maeda K., 2004, The Scalar-Tensor Theory of Gravitation. Cambridge University Press, Cambridge, UK
Drimmel R., Poggio E., 2018, Res. Notes AAS, 2, 210
Eilers A. C., Hogg D. W., Rix H. W., Ness M. K., 2019, ApJ, 871, 120
Einstein A., 1905, Ann. of Phys., 17, 891
Everall A. et al., 2019, MNRAS, 489, 1, 910
Fitz Gerald G. F., 1889, Science, 13, Issue 328, p. 390
Frigerio M. C., Lima J. A. S., Chimenti P., 2015, MNRAS, 449, 3645
Gaia Collaboration, Prusti T., de Bruijne J. H. J., Brown A. G. A., Vallenari A. , Babusiaux C., Bailer-Jones C. A. L., Bastian U., Biermann M., Evans D. W. et al., 2016, The Gaia mission, A&A, 595, A1
Gaia Collaboration, Brown A. G. A., Vallenari A. , Prusti T., de Bruijne J. H. J., Babusiaux C., Bailer-Jones C. A. L. et al., 2018, Gaia Data Release 2. Summary of the contents and survey properties, A&A, 616, A1
Gaia Data Release 1 Documentation version 1.2 , 2017
Garbari S., Liu C., Read J. I., Lake G., 2012, MNRAS, 425, 1445
GRAVITY collaboration et al., 2018, A&A, 615, L15
GRAVITY collaboration et al., 2018, A&A, 618, L10
Grumiller D., Balasin H., Preis, F., 2008, European Space Agency, the Advanced Concepts Team, Ariadna Final Report (07-1301)
Iocco F., Pato M., Bertone G., 2015, Nature Phys., 11, 245
Iocco F., Pato M., Bertone G., Jetzer P., 2011, J. Cosmol. Astropart. Phys., 11, 29
Jeans J. H., 1915, MNRAS, 76, 70
Katz D. et al., 2019, A&A, 622, A205
Korol V., Rossi E. M., Barausse E., 2019, MNRAS, 483, 5518
Lense J., Thirring H., 1918, Physikalische Zeitschrift, 19, 156
Lynden-Bell D., Katz J., Bičák B., 1995, MNRAS, 272, 150
Liu J. et al., 2019, Nature, 575, 618
Magalhaes N.S., Cooperstock F.I., 2017, Astrophys. Space Sci, 362, 210
Mathematica, Version 9.0, 2012, Wolfram Research, Inc., Champaign, IL
McKee C. F., Parravano A., Hollenbach D.J., 2015, ApJ, 814, 13
McMillan P. J., 2017, MNRAS, 465, 76
Mignard F. et al., 2018, A&A, 616, A14
Milgrom M., 1983, ApJ, 270, 365
Moni Bidin C., Smith R., Carraro G., Méndez R. A., Moyano M., 2015, A&A, 573, A91
Navarro J. F., Frenk C. S., White S. D. M., 1996, ApJ, 462, 563
Nazari E. et al., 2017, ApJ, 839, 75
Neill C., 2011, MAPH480 Project Report, Supervisors: Prof. David L. Wiltshire, Dr. Teppo Mattsson, University of Canterbury, Dep. of Phys. and Astron., Christchurch, New Zeland
Neugebauer G., Meinel R., 1995, Phys. Rev. Lett., 75, 3046
Neugebauer G., Kleinwächter A., Meinel R., 1996, Phys. Acta, 69, 472 (revised online version: arXiv:gr-qc/0301107)
Padmanahan T., 2010, Gravitation. Foundation and Frontiers. Cambridge University Press, Cambridge, UK
Poisson E., Will C.M., 2014, Gravity. Cambridge University Press, Cambridge, UK
Poggio E., Drimmel R., Lattanzi M.G., Smart R. et al., 2018, MNRAS, 481, Issue 1, L21
Pouliasis E., Di Matte P., Haywood M., 2017, A&A, 598, A66
Re Fiorentin P., Lattanzi M. G., Spagna, A., 2019, MNRAS, 484, Issue 1, L69
Rubin V. C., Thonnard N., Ford Jr. W. K., 1978, ApJ, 225, L107
Salvatier J., Wiecki T.V., Fonnesbeck C., 2016, PeerJ Comp. Sci., 2:e55
Skrutskie M. F. et al., 2006, AJ, 131, 1163
Smith H. Jr, Eichhorn H., MNRAS, 281, 211
Starobinsky A. A., 1980, Phys. Lett. B, 91, 99
Stephani H., Kramer D., Maccallum M., Hoenselaers C., Herl E., 2009, Exact Solutions of Einstein's Field Equations. Cambridge University Press, Cambridge, UK
Tsallis C., 1988, J. Stat. Phys., 52, 479
Tsallis C., Arenas Z.G., 2014, in Bravin L., FokaY., Kabana S., eds, Proc. 2nd International Conference on New Frontiers in Physics, EPJ Web of Conferences, 71, id. 00132
Van Stockum W. J., 1937, in Proc. R. Soc. Edinb. A 57, 135
Wald R. M., 1984, General Relativity. University of Chicago Press, Chicago, USA
Watanabe S., 2010, J. Mach. Learn. Res., 11, 3571(Zbl 1242.62024)
Zingg T., Aste A., Trautmann D., 2007, Adv. Stud. Theor. Phys. 1, 409
Zwicky F., 1937, ApJ, 86, 217

APPENDIX A: THEORETICAL BACKGROUND

It is known that, in a stationary and axisymmetric space-time there exist two commuting Killing vector fields, k^α (time-like) and m^α (always zero on the axis of symmetry), and a coordinate system $\{t, \phi, r, z\}$ adapted to the symmetries (de Felice & Clarke 1990; Stephani et al. 2009; Stockum 1937), whose line element for a rotating perfect fluid takes the form:

$$ds^2 = -e^{2U}(dt + Ad\phi)^2 + e^{2U}\left(e^{2\gamma}(dr^2 + dz^2) + Wd\phi^2\right), \quad \text{(A1)}$$

where $e^{2U}, e^{2\gamma}$ are conformal factors and U, A, W depend only one the coordinates $\{r, z\}$. The time coordinate t (time-like far enough from the metric source) spans the range $[-\infty, +\infty]$ and ϕ is the azimuthal angular coordinate in the interval $[0, 2\pi]$ (de Felice & Clarke 1990). For the general dust solution (Stephani et al. 2009, eq. (21.50)) we have:

$$-e^{2U} = (k|k),\ -Ae^{2U} = (k|m),\ e^{-2U}W^2 - A^2e^{2U} = (m|m). \quad \text{(A2)}$$

In addition

$$m^\alpha = \partial^\alpha_\phi,\ k^\alpha = \partial^\alpha_t,\ \partial_t g_{ij} = \partial_\phi g_{ij} = 0,\ g_{\phi a} = g_{ta} = 0, \quad \text{(A3)}$$

where $a = r, z$. Because of the two dimensional Laplace equation one can choose $W = r^2$.

For rigidly rotating dust (i.e. shear-free and expansion-free), one can choose $U = 0$ and there exist a time-like Killing vector (linear combination of k^α and m^α with a constant coefficient) parallel to the four-velocity of the fluid u^α, i.e. the co-rotating one chosen by Balasin & Grumiller (2008), proportional to ∂^α_t (Stephani et al. 2009). Then, by setting $e^{2\gamma} \equiv e^\nu$, $N = -A$ and $e^{2U} = 1$, eq. (A1) becomes the line element adopted by Balasin & Grumiller (2008).

APPENDIX B: DETAILS ON THE PARAMETERS AND PRIORS OF THE FIT

The parameter space is too large to explore with a simple nonlinear fit. We therefore decided to use the Markov Chain Monte Carlo (MCMC) method to determine the unknown parameters and their uncertainties (see sec. 3.3). Actual computations made use of the MCMC python package PyMC3 (Salvatie et al. 2016) with the NUTS algorithms chosen for the step selection. To explore the full pdf we implement the following priors:

- *BG model* : (i) Uniform for $V_0 \in [150, 300]$ km/s; (ii) Uniform for $R_{out} \in [10, 100]$ kpc; (iii) Uniform for $r_{in} \in [0, 2]$ kpc; (iv) Uniform for $e^{\nu_0} \in [0.001, 10]$[10] ;

[10] This is the value characterizing our approximation of a constant metric conformal factor, i.e., $e^{\nu(R,z)} \approx e^{\nu_0}$.

• *MWC model* : (i) Normal for $M_b = \mathcal{N}(\mu = 1.067, \sigma = 0.5)\, 10^{10} \mathrm{M}_\odot$; (ii) Normal for $M_{td} = \mathcal{N}(\mu = 3.944, \sigma = 0.5) 10^{10}\, \mathrm{M}_\odot$; (iii) Normal for $M_{Td} = \mathcal{N}(\mu = 3.944, \sigma = 0.5) 10^{10}\, \mathrm{M}_\odot$; (iv) Normal for $a_{td} = \mathcal{N}(\mu = 5.3, \sigma = 0.5)$ kpc; (v) Normal for $a_{Td} = \mathcal{N}(\mu = 2.6, \sigma = 0.5)$ kpc; (vi) Normal for $\rho_0^{halo} = \mathcal{N}(\mu = 0.01, \sigma = 0.005)\, \mathrm{M}_\odot \mathrm{pc}^{-3}$; (v) Normal for $A_h = \mathcal{N}(\mu = 19.6, \sigma = 4.9)$ kpc.

In addition, in the MWC model, we fix $b_b = 0.3$ kpc (Pouliasis, Di Matte & Haywood 2017), as our data do not explore the galactic central region where the bulge dominates. In this way, we eliminate any possible correlations with the free parameters. We stress that we use normal pdf priors for the MWC model, so that we can compare our bayesian analysis to the most recent observational estimates (see second bullet above). On the other hand, for the BG free parameters we adopted uniform prior distributions as there is no previous knowledge for such parameters, being this the first time of a fit to a general relativistic model with data for the Milky Way. We also fix $b_{td} = 0.25$ kpc and $b_{td} = 0.8$ kpc (Pouliasis, Di Matte & Haywood 2017), as in our work we neglect the vertical data distribution, and consider only binned radial rings. For the MWC model, the estimated parameters are, within the errors, compatible with literature values (Iocco et al. 2011; Bovy 2015; McMillan 2017; Pouliasis, Di Matte & Haywood 2017; Korol, Rossi & Barausse 2019). The largest contributions to the 1σ confidence interval come from M_b and A_h uncertainties, which are the most difficult to constrain because of the relatively narrow range covered by the DR2 data.

APPENDIX C: THE GOODNESS OF THE ANALYSIS AND POSTERIOR CORRELATIONS

Figure 1 shows the two estimated velocity profiles that are both good representations of the observed (binned) data. To quantitatively asses this, we compare the two models via the Widely Applicable Information Criterion (WAIC, Watanabe, 2010), which is a fully Bayesian criterion for estimating the out-of-sample expectation.

By definition, lower values of the WAIC indicate a better fit, i.e, the WAIC measures the *poorness* of the fit. Our MCMC runs result in the values 288.8 and 282.6 for the BG and MWC models, respectively. Therefore, for our likelihood analysis the two models appear almost identically consistent with the data.

Furthermore, Figures C1 and C2 show the posterior distributions of the parameters for the MWC and BG model, respectively. For the MWC model, the strongest correlation is between the DM halo scale density ρ_0^{halo} and its radial scale A_h, similarly to (McMillan 2017). There are smoother correlations between all the other parameters. Moreover, means and medians are always practically coincident (compare with the mean values reported in Table 3 of sec. 3.3); therefore, they can both be used in the distribution of their respective posterior.

On the other hand, for the BG model the results suggest stronger correlations or anticorrelations between the radial (r_{in}, R_{out}) parameters and the velocity normalization V_0. This is reasonable based on their definitions (see sec. 3.3). The conformal factor constant e^{ν_0} appears to be less correlated with the other parameters. This is somewhat expected, as this parameter does not enter in the expression for the BG rotational velocity, and can only be estimated thanks to the direct use of the BG density function (16) in the likelihood expression (15) (again see sec. 3.3). Analogously to the MWC model case, for the BG model as well means and medians are fairly comparable (see Table 2 in sec. 3.3). Finally, we report in tables C1, C2, C3, and C4 numerical evidence that the implementation of the Jeans correction, i.e. the use of V_{circ} instead of V_ϕ data, has not much influence on the posteriors estimates in both models.

BG V_ϕ	V_0	R_{out}	r_{in}	e^{ν_0}
hpd 0.16	246.67	33.07	0.13	0.07
median	262.35	45.27	0.39	f 0.08
hpd 0.84	289.04	71.84	0.74	0.10

Table C1. Posterior estimates for the BG model using V_ϕ data. hpd stands for "highest posterior density" and is the minimum width Bayesian credible interval.

BG V_{circ}	V_0	R_{out}	r_{in}	e^{ν_0}
hpd 0.16	250.48	38.33	0.27	0.07
median	269.22	53.28	0.55	0.08
hpd 0.84	289.21	92.83	0.81	0.10

Table C2. Same as in Table C1 but for V_{circ} computed with the implementation of the Jeans correction.

MCW V_ϕ	M_b	M_{td}	M_{Td}	a_{td}	a_{Td}	ρ_0^{halo}	A_h
hpd 0.16	0.65	3.49	3.56	4.70	2.30	0.61	13.61
median	1.01	3.89	4.01	5.16	2.68	0.87	16.75
hpd 0.84	1.37	4.28	4.47	5.63	3.08	1.23	20.74

Table C3. Same as in Table C1 but for the MWC model. Note that ρ_0^{halo} is in unit of $10^2\, \mathrm{M}_\odot\, \mathrm{pc}^{-3}$.

MCW V_{circ}	M_b	M_{td}	M_{Td}	a_{td}	a_{Td}	ρ_0^{halo}	A_h
hpd 0.16	0.54	3.49	3.52	4.79	2.40	0.69	14.05
median	0.90	3.88	3.98	5.25	2.79	0.95	17.02
hpd 0.84	1.25	4.27	4.43	5.71	3.19	1.32	20.75

Table C4. Same as in Table C2 but for the MWC model. Note that ρ_0^{halo} is in unit of $10^2\, \mathrm{M}_\odot\, \mathrm{pc}^{-3}$.

APPENDIX D: THE EINSTEIN FIELD EQUATIONS

Solving Einstein's equation translates into a system of coupled nonlinear partial differential equations, and for that there exist no general method to obtain all of the solutions.

Namely, considering line element (4) and tensor $T_{\alpha\beta} = \rho g_{\alpha\mu} g_{\beta\tau} u^\mu u^\tau$ (in virtue of the definition of $T^{\alpha\beta}$, and in the limit of small density, u^α results geodetic), one obtains the following expression for the Einstein field equations:

$$r\partial_z \nu + \partial_r N \partial_z N = 0 \quad \text{(D1)}$$

$$2r\partial_r \nu + (\partial_r N)^2 - (\partial_z N)^2 = 0 \quad \text{(D2)}$$

$$2r^2(\partial_r\partial_r \nu + \partial_z\partial_z \nu) + (\partial_r N)^2 + (\partial_z N)^2 = 0 \quad \text{(D3)}$$

$$r(\partial_r\partial_r N + \partial_z\partial_z N) - \partial_r N = 0 \quad \text{(D4)}$$

$$(\partial_r N)^2 + (\partial_z N)^2 = kr^2 \rho e^\nu \quad \text{(D5)}$$

By solving this system of PDE's one recovers the functions

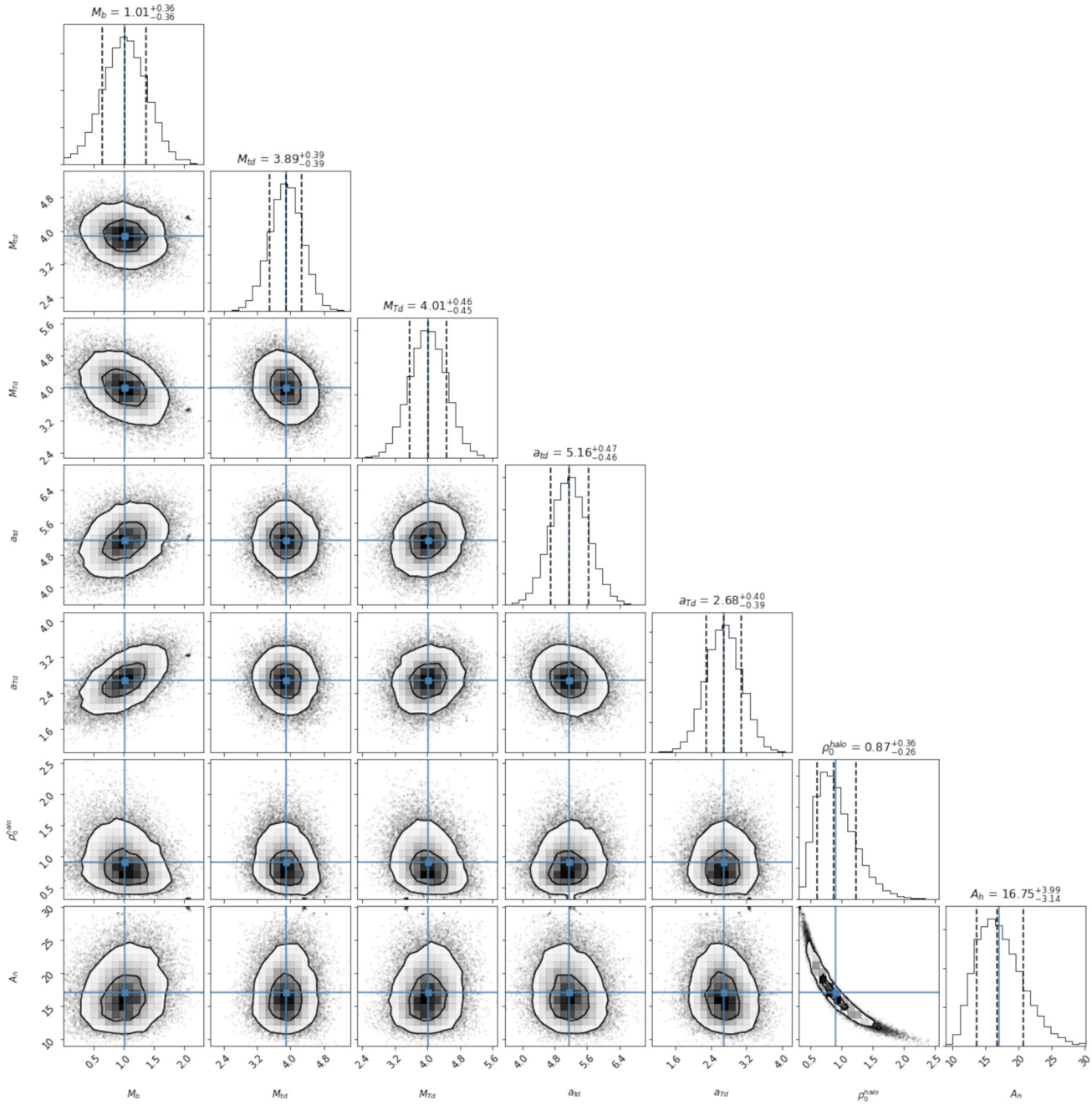

Figure C1. MWC parameters corner plot. The one-dimensional (histogram) posterior distributions of each parameter are shown on the diagonal of the drawing, while the other panels represent the two-dimensional (contours) correlations. The black thick contours indicate the 1 and 2 σ credible levels, while the blue squares represent the mean value of each posterior distribution. The black dashed vertical lines mark the 16th, 50th (i.e. median) and 84th percentiles of the posterior. Finally, the average values and their corresponding 16th and 84th percentiles are shown on top of the histograms. Note that ρ_0^{halo} is in unit of $10^2\,M_\odot\,pc^{-3}$.

$N(r,z)$, $\nu(r,z)$ (see sections 2.3 and 2.4 in Balasin & Grumiller, 2008), and via equation (D5) we compute the local mass density.

This paper has been typeset from a TEX/LATEX file prepared by the author.

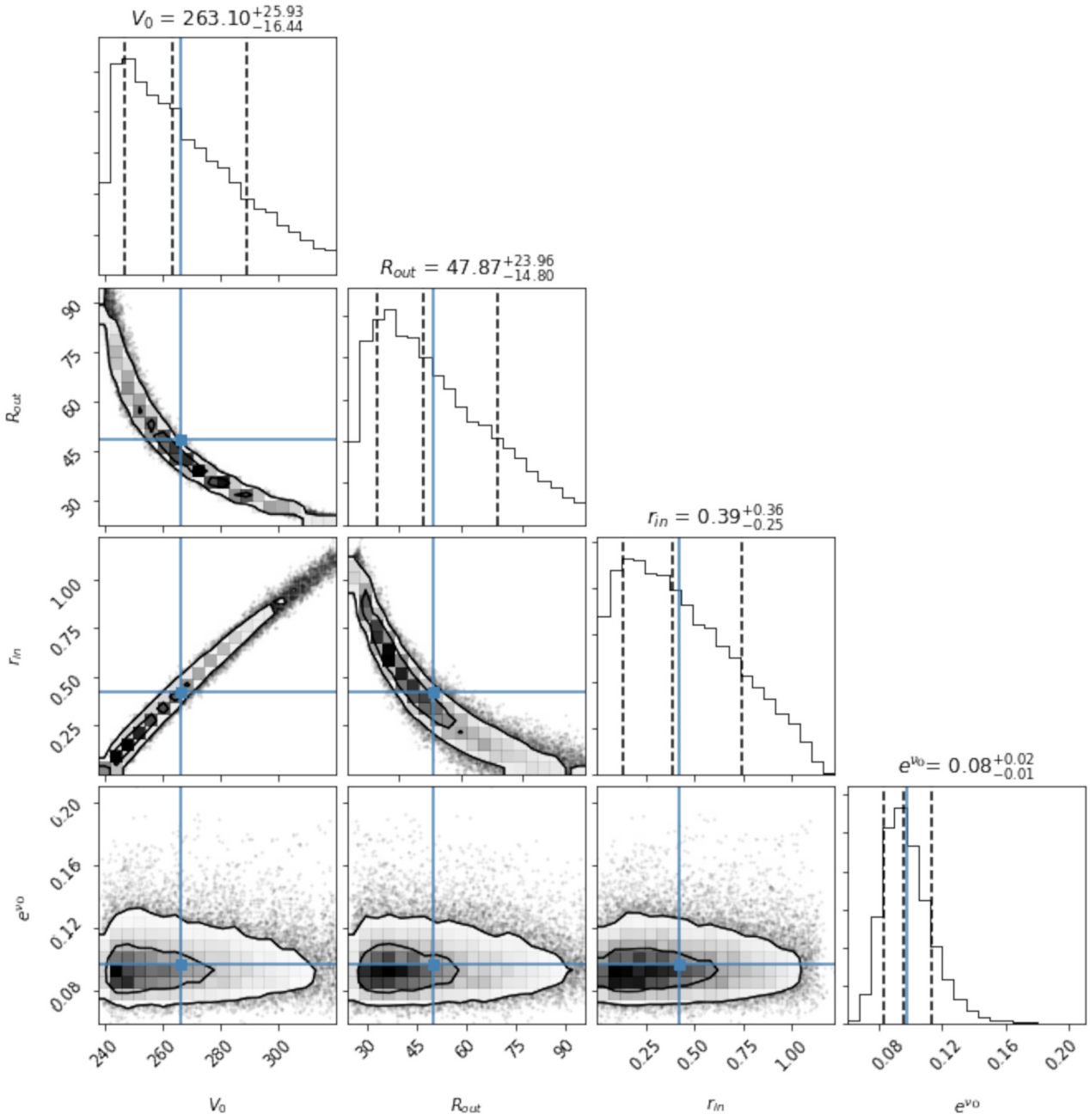

Figure C2. BG parameters corner plot. Same as in Figure C1.